13. LLE Rev. **24**, 169 (1985); C. Fievet, Thèse de Doctorat, Paris XI University, Orsay, France, 1989, quoted in C. Chenais-Popovics *et al.*, *Phys. Rev. A* **40**, 3194 (1989).

14. H. A. Bethe and E. E. Salpeter, *Quantum Mechanics of One- and Two-Electron Atoms* (Plenum, New York, 1977), pp. 297, 305, 316.

15. H. A. Kramers, *Philos. Mag.* **46**, 836 (1923); J. A. Gaunt, *Philos. Trans. R. Soc. London A* **229**, 163 (1930).

16. D. H. Menzel and C. L. Pekeris, *Mon. Not. Roy. Astron. Soc.* **96**, 77 (1935).

17. E. J. McGuire, *Phys. Rev.* **185**, 1 (1969).

18. C. P. Bhalla and T. W. Tunnell, *J. Quant. Spectrosc. Radiat. & Transfer* **32**, 141 (1984).

19. H. A. Bethe and E. E. Salpeter, *ibid.*, pp. 251, 266.

20. H. R. Griem, *Plasma Spectroscopy* (McGraw-Hill, New York, 1964), p. 147.

21. W. Lotz, *Z. Phys.* **216**, 241 (1968), quoted in D. Salzmann and A. Krumbein, *J. Appl. Phys.* **49**, 3229 (1978).

22. H. R. Griem, *ibid.*, p. 112, quoted in R. Epstein, S. Skupsky, and J. Delettrez, *J. Quant. Spectrosc. Radiat. & Transfer* **35**, 131 (1986).

23. E. J. McGuire, *Phys. Rev. A* **2**, 273 (1970).

1.B Transverse Instabilities of Counterpropagating Light Waves

Instabilities of Counterpropagating Waves in ICF

Direct-drive laser fusion requires high-gain fusion pellets to overcome the inherent losses associated with initiating the inertial fusion process. Conversion of laser light into energy used to drive the compression of the fuel pellet begins in the corona where the intense laser field must penetrate a plasma and deposit its energy into the pellet material. Two critical aspects of this deposition process are (1) the laser absorption efficiency and (2) the implosion symmetry.[1,2]

In the direct-drive fusion process both absorption efficiency and implosion symmetry can be adversely affected by parametric and focusing instabilities that occur during the interaction of the laser light with the coronal plasma. Focusing instabilities can degrade the uniformity of the laser light as it passes through the corona by enhancing modulations of the laser profile and distributing the incident laser light into filaments. This nonuniform deposition of laser energy can seed hydrodynamic instabilities that further degrade the laser-to-fuel coupling efficiency and inhibit the fusion gain.

Parametric instabilities can degrade the absorption of laser light by scattering it away from the pellet. More importantly, they are one source of hot electrons that can divert energy from the ablation process and preheat the fuel.

In this article, we discuss parametric and focusing instabilities arising because of the coupling of laser light to ion modes.[3,4] Though recent studies have shown that shorter-wavelength lasers[5] significantly reduce the effect of these instabilities, there is still much to be learned about their role in reactor-size plasmas. In addition to being important in ICF, these instabilities play a fundamental role in the interaction of laser light with other nonlinear optical materials and are of general interest.

Parametric and focusing instabilities need not occur in isolation. In fact, Brillouin scattering and filamentation are known to be closely related,[3,4] and recent studies have shown a correlation between the generation of Brillouin-scattered light and Raman-scattered light.[6–8] This article contains a description of a preliminary study of the transverse modulational instability in a plasma with adiabatic ion response when feedback from a counterpropagating wave is present. Several researchers have studied the effects of back-scattered or back-reflected light on parametric instabilities in laser-produced plasmas.[9–11] The backward propagating light may arise because of reflection of the incident laser from the critical surface, parametric back-scattering, or shinethrough, as shown in Fig. 46.2. In related applications, such as optical phase conjugation and x-ray lasers, the counterpropagating laser field is externally applied.

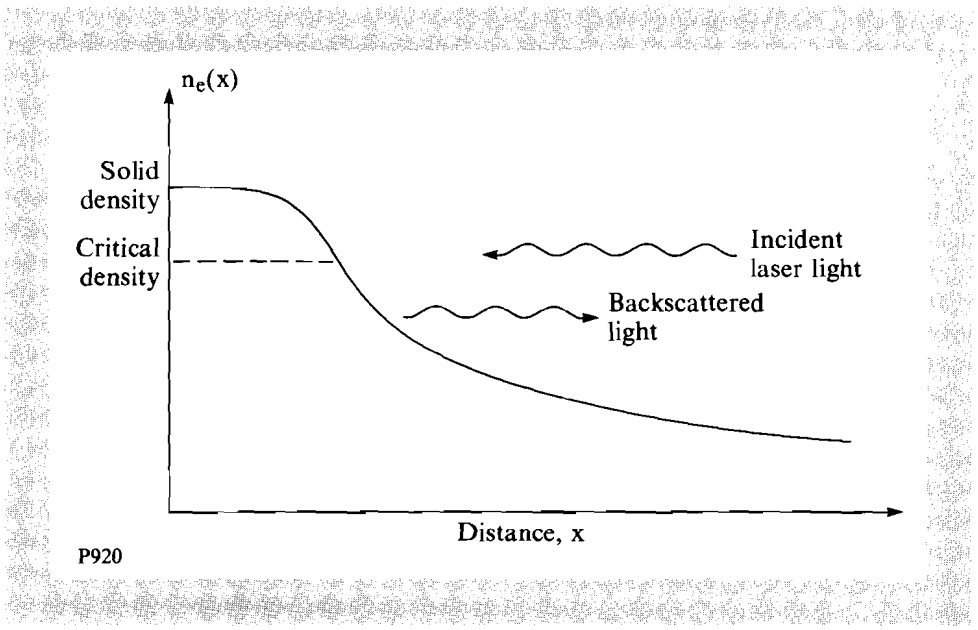

Fig. 46.2
Feedback from light propagating back towards the incident laser can arise from several sources.

Studies on the effect of counterpropagating laser fields in plasmas are closely related to basic nonlinear optics research in which the effect of a counterpropagating laser beam on parametric scattering and four-wave mixing has been investigated.[12,13] In addition, researchers in nonlinear optics have investigated the effect of a counterpropagating laser beam on transverse modulational instabilities in nonresonant media.[14–20] This work on nonresonant transverse modulational instabilities has been extended to include the resonant effects of the ion-acoustic response of a plasma. Though the model discussed here is simplified with respect to laser-plasma interactions, it is expected to be of direct relevance to the study of basic physics in, and applications of, nonlinear optical systems. In addition, this work provides a solid starting point for further laser-plasma interaction research.

Four-Sideband Instabilities

In this section the dominant interactions in the counterpropagating-wave system are introduced. A pair of intense, counterpropagating light waves, of frequency ω_0 and wave vector $\pm\boldsymbol{k}_0$, irradiate opposite ends of a homogeneous plasma of length L. Let $\boldsymbol{F}_0$ be the amplitude of the intense pump wave injected at the left end of the plasma, while $\boldsymbol{B}_0$ is the amplitude injected from the right end of the plasma. At high intensity, the ions respond to the presence of the light fields. Thus, since the index of refraction of the plasma is a function of the plasma density, it responds to the intensity of the fields on the ion-acoustic time scale.

Small-amplitude sidebands of the intense counterpropagating light waves can arise in the system as a result of noise within the plasma or by injection from an external source. Consider a single, small-amplitude, anti-Stokes sideband $\mathbf{F}_+$, which has frequency $\omega_0 + \omega$ and wave vector $\boldsymbol{k}_0 + \boldsymbol{k}$ as shown in Fig. 46.3. This sideband can interfere with the pump fields, creating periodic variations in the intensity that drive a grating in the index of refraction. In a plasma, these gratings can be driven at the frequency and wave number of the ion-acoustic wave. Since the ion-acoustic wave is a natural mode of the plasma, the gratings can be driven resonantly. Once a grating is formed, the pump fields can scatter from it to augment the sidebands.

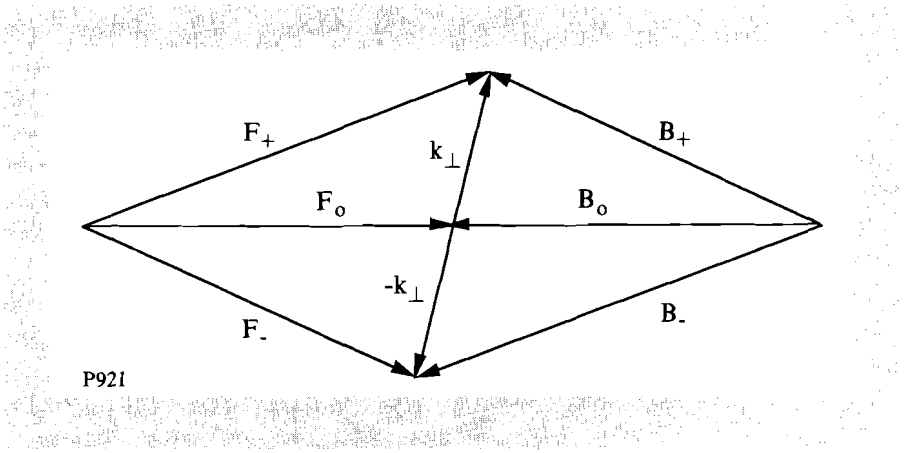

Fig. 46.3
The wave-vector matching diagram for the four-sideband interaction.

One distinct set of sidebands grows more strongly than the others. The phases of these modes are tuned in such a way that their linear and nonlinear phase shifts are optimally matched inside the medium. As a result, these optimally phase-matched modes exchange energy with the pump fields more efficiently than the unmatched modes can. In many instances these phase-matched sidebands are unstable. The counterpropagating-wave interaction can support two types of instabilities. At moderate intensity sidebands can grow as they propagate and are said to be convectively unstable. At higher intensity unstable sidebands can grow exponentially in time at each point in the plasma. This latter form of instability is called an absolute instability and grows in the frame of the medium without convecting away.

In the counterpropagating-wave system the two pump waves interact most strongly with a set of four sidebands that lie in a plane that includes the pump axis. Thus, the $\boldsymbol{F}_+$ sideband couples most strongly to the three other sidebands shown in Fig. 46.3. It couples with the Stokes-shifted sideband $\boldsymbol{F}_-$ as a result of a forward four-wave mixing process. It couples with the anti-Stokes sideband $\boldsymbol{B}_+$ as a result of Bragg reflection, and it couples with the Stokes-shifted sideband $\boldsymbol{B}_-$ as a result of a backward four-wave mixing process. In this article the linear stability of the four-sideband interaction is of primary interest, so let $|\boldsymbol{F}_0|, |\boldsymbol{B}_0| \gg |\boldsymbol{F}_\pm|, |\boldsymbol{B}_\pm|$. This system is expected to be coupled most strongly when the sidebands are polarized parallel to one another and to the pump waves, so let each wave be linearly polarized parallel to each of the other waves.

Growth of the four sidebands can occur as a result of several different fundamental interactions. The pure four-sideband interaction results from the concurrent interaction of all four sidebands with the pumps and occurs when the two oppositely propagating pump fields and the four sidebands are all simultaneously phase matched. This interaction is a true four-sideband resonance. As this four-sideband resonance is detuned, four two-sideband interactions are recovered.

The two-sideband forward four-wave mixing process occurs when a single pump field couples to a Stokes and an anti-Stokes sideband. Both sidebands propagate in the same direction as the pump field, but each sideband has a small perpendicular wave-number component. Thus, the $\boldsymbol{F}_+$ sideband couples with the pump $\boldsymbol{F}_0$ to drive a grating at $(\omega,\boldsymbol{k}_\perp)$. The $\boldsymbol{F}_0$ pump then scatters off of this grating to create the $\boldsymbol{F}_-$ sideband as shown in Fig. 46.4(a). Note that in general the wave-vector shift of the sideband need not be small and perpendicular with respect to the pump wave vectors. However, since the most important near-axis scattering processes obey this restriction, the more general cases are neglected for the purposes of this article.

Taken together, this pair of sidebands is equivalent to a transverse spatial modulation of the light-wave intensity profile. Since the index of refraction increases with increased intensity, a positive feedback loop is created between the field intensity and the medium. As a result, these transverse modulations grow as the interaction proceeds. This near-forward scattering

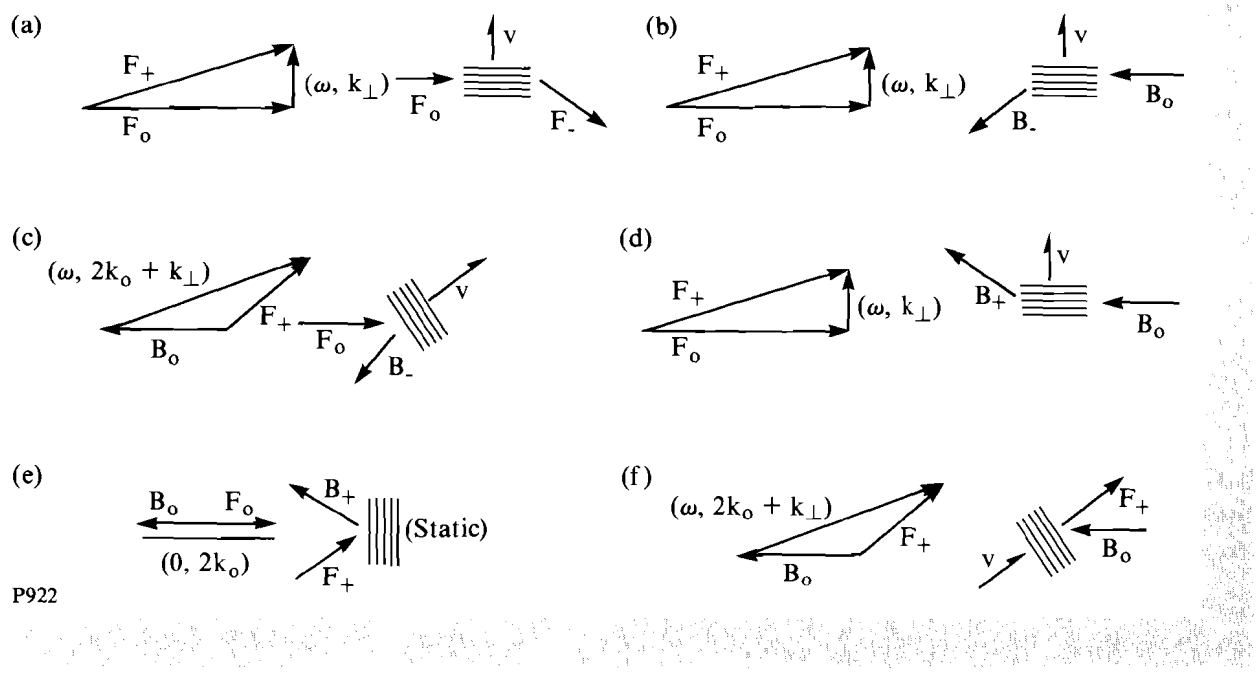

Fig. 46.4
Each two-sideband interaction is shown. (a) Forward four-wave mixing from the short wave-number grating, (b) backward four-wave mixing, (c) backward four-wave mixing from the static $2k_0$ grating, (d) backward phase conjugation from the short-wavelength grating, (e) backward phase conjugation from the long-wavelength grating, and (f) forward four-wave mixing from the large wave-number grating.

instability is the transverse modulational instability, and is associated with filamentation and self-focusing in its fully nonlinear manifestation. The transverse modulational instability has a dominant band of unstable transverse perturbation wave numbers. As a result, the transverse spatial Fourier spectrum of the scattered light will contain sidebands centered on the optimal transverse perturbation wave number or equivalently at the optimal cone angle. These sidebands are a signature of the instability. Thus, the transverse modulational instability can be thought of as self-induced diffraction. Since this interaction is invariant to rotations about the collinear pump axis, a probe sideband injected at any point on the circle determined by the cone angle will result in the appearance of a signal sideband located exactly opposite the probe on the same circle. When this convective instability is seeded by noise, all orientations of the sidebands are seeded equally and conical emission occurs.

Two different two-sideband backward four-wave mixing processes can also occur. Phase conjugate backward four-wave mixing occurs when a pair of oppositely propagating pump fields couple to a Stokes and anti-Stokes sideband that propagate exactly opposite to each other as shown in Figs. 46.4(b) and 46.4(c). This phase-conjugate coupling has been studied extensively in the past. Recall that as the intensity of the pump fields is increased, the phase-conjugate interaction becomes absolutely unstable. A less important backward four-wave mixing process occurs when a pair of oppositely propagating pump fields couple to a pair of oppositely propagating Stokes or anti-Stokes sidebands as shown in Figs. 46.4(d) and 46.4(e). This process corresponds to Bragg reflection.

Finally, a Stokes or anti-Stokes sideband can couple to the oppositely propagating pump to drive a short-wavelength grating as shown in Fig. 46.4(f). The same pump that drives the grating can scatter from the grating to enhance the sideband with which it is coupled. Note that either the Stokes or anti-Stokes sideband can couple with the oppositely propagating pump field. This interaction is stimulated Brillouin scattering and requires the ion-acoustic grating to be driven resonantly. In a plasma each of the two sideband interactions is enhanced near the ion-acoustic resonance. Resonantly enhanced four-wave mixing and phase conjugation in plasmas is of great current interest.[21] In addition, some researchers have begun to investigate resonant self-focusing in plasmas.[22]

Origin of the Four-Sideband Equations

In this section the origin of the governing equations for the four-sideband interaction is discussed. A model describing the coupling of the transverse electromagnetic fields of two light waves propagating in a quasi-neutral plasma can be developed with Maxwell's equations when they are coupled to the two-fluid equations of motion for the plasma. The fluid equations take the form

$$\partial_t n_s + \nabla \cdot (n_s \boldsymbol{V}_s) = 0,$$

$$\partial_t \boldsymbol{V}_s + (\boldsymbol{V}_s \cdot \nabla)\boldsymbol{V}_s = -\nabla P_s / n_s m_s + q_s(\boldsymbol{E} + \boldsymbol{V}_s \times \boldsymbol{B}/c)/m_s,$$

where the subscript s denotes the particle species (electron or ion). $\boldsymbol{V}_s$ is the velocity field of one plasma species, P_s is the pressure, and q_s is the particle charge. The charge and current densities that drive Maxwell's equations are

$$\rho = \sum_s n_s q_s, \quad \boldsymbol{J} = \sum_s n_s q_s \boldsymbol{V}_s,$$

respectively. In equilibrium, $n_e(0) = Zn_i(0) = n_0$, where Z is the ionization number and $\boldsymbol{V}_e(0) = \boldsymbol{V}_i(0) = 0$. It can be seen from the momentum equation that the first-order electron motion is in the direction of the applied electric field. Thus

$$\boldsymbol{V}_\perp = e\boldsymbol{A}_\perp / m_e c,$$

where $\boldsymbol{A}_\perp$ is the transverse component of the vector potential. Assuming that the low-frequency plasma evolution is quasi-neutral, then $n_e^{(1)} \approx Zn_i^{(1)}$, and the following set of equations governing the evolution of $\boldsymbol{V}_\perp$ and $\langle n \rangle = n_e^{(1)}/n_0$ arises from the root equations

$$\left[\partial_{tt} + \omega_e^2 - c^2\nabla^2\right]\boldsymbol{V}_\perp = -\omega_e^2 \langle n \rangle \boldsymbol{V}_\perp$$

$$\left[\partial_{tt} - 2i\gamma\partial_t - c_s^2\nabla^2\right]\langle n \rangle = Ze^2\nabla^2\left\langle \boldsymbol{V}_\perp^2 \right\rangle / 2c^2 m_e m_i,$$

where $\langle\ \rangle$ denotes an average over the high-frequency components, $c_s^2 = Z T_e^{(0)}/m_i$ is the ion-sound speed, and $T_e^{(0)}$ is the equilibrium electron

temperature. The first equation is the analog of Maxwell's wave equation for the electric field driven by the time derivative of the material polarization. The second equation is the sound-wave equation driven by the low-frequency variations in light pressure.

The dependent variable $\boldsymbol{V}_\perp$ varies on the fast time scale of the electromagnetic fields and on the slow time scale of the ions. This variable represents the total field and can be written

$$\boldsymbol{V}_\perp = (1/2)(\boldsymbol{F}_0 + \boldsymbol{F}_+ + \boldsymbol{F}_-)\exp[i(\boldsymbol{k}_0 \cdot \boldsymbol{x} - \omega_0 t)]$$

$$+(1/2)(\boldsymbol{B}_0 + \boldsymbol{B}_+ + \boldsymbol{B}_-)\exp[i(-\boldsymbol{k}_0 \cdot \boldsymbol{x} - \omega_0 t)] + c.c.,$$

where the wave amplitudes vary slowly in space and time with respect to the scales k_0 and ω_0. Recall that for the linear stability analysis $|\boldsymbol{F}_0|$, $|\boldsymbol{B}_0| \gg |\boldsymbol{F}_\pm|, |\boldsymbol{B}_\pm|$, and the intensities of the pump waves are constant. The linearized equations can then be Fourier transformed in the transverse direction and Laplace transformed over time. When the light-wave amplitudes vary slower than $\langle n \rangle$, the plasma reacts to variations in the fields almost instantaneously. The sound-wave equation becomes

$$\langle n \rangle(\omega, k) = \Gamma(\omega, k)\left\langle \boldsymbol{V}_\perp^2 \right\rangle_L ,$$

where

$$\Gamma(\omega, k) = \left(\omega_e^2/8\omega_0\right)\left[c_s^2 k^2 / \left(c_s^2 k^2 - 2i\gamma\omega - \omega^2\right)\right],$$

and $\langle \boldsymbol{V}_\perp^2 \rangle_L$ contains only linear terms. The line function $\Gamma(\omega, k)$ characterizes the ion-acoustic response of the plasma to the ponderomotive force of the fields. The Fourier transform over the transverse coordinates is equivalent to letting the sidebands $\boldsymbol{F}_\pm$ and $\boldsymbol{B}_\pm$ vary such that

$$|\boldsymbol{F}_\pm| \propto \exp[\pm i\boldsymbol{k}_\perp \cdot \boldsymbol{r}]$$

$$|\boldsymbol{B}_\pm| \propto \exp[\pm i\boldsymbol{k}_\perp \cdot \boldsymbol{r}].$$

In the limit $|\boldsymbol{k}_\perp/\boldsymbol{k}_0| \ll 1$, $\theta \approx |\boldsymbol{k}_\perp/\boldsymbol{k}_0|$ constitutes the small angle or paraxial approximation and restricts this analysis to near-forward and near-backward scattering.

Finally, by keeping only the electromagnetic modes driven resonantly, the linearized equations governing the interaction of the four sidebands are obtained. They take the form

$$LA = MA$$

where $\boldsymbol{A} = (F_-^*, F_+, B_-^*, B_+)^T$ and $L_{ij} = (-\omega \pm i\nu d_x - ck_\perp^2/2k_0)\,\delta_{ij}$. The coupling terms M_{ij} are proportional to $\Gamma(\omega,k)$ and the pump intensities. Each coupling term corresponds to one of the refractive-index gratings that mediate the

interaction of the sidebands. These gratings have components $\langle n\rangle(\omega, 2\boldsymbol{k}_0 \pm \boldsymbol{k}_\perp)$, $\langle n\rangle(\omega, \pm\boldsymbol{k}_\perp)$ and $\langle n\rangle(0, 2\boldsymbol{k}_0)$ along with their complex conjugates. Some of these gratings are shown in Fig. 46.4. Note that the terms ω and $k_\perp^2/2k_0$ act as the linear phase shifts while the M_{ij} correspond to the nonlinear phase shifts.

Convective Gain Spectrum

The four-sideband equations are a system of four coupled complex linear equations. From these equations information about the stability of the four-sideband interaction can be obtained. The convective gain spectrum is obtained by solving these equations as a two point boundary value problem with $B_\pm(L)$ and $F_-(0)$ equal to zero and $F_+(0)$ set at a finite constant value δ. As shown in Fig. 46.5, this process is equivalent to scattering the probe sideband $F_+(0)$ from the system into the four sidebands. In Figs. 46.6(a)–46.6(d) the convective gain of these four sidebands is plotted as a function of $k_\perp^2 L/2k_0$ and $\omega L/v$, where v is the group velocity of the light waves in the plasma. In these plots the gain is scaled to the size of the input probe δ and the pump intensity is 0.92 of the minimal absolute threshold intensity where $|B_0| = |F_0|$.

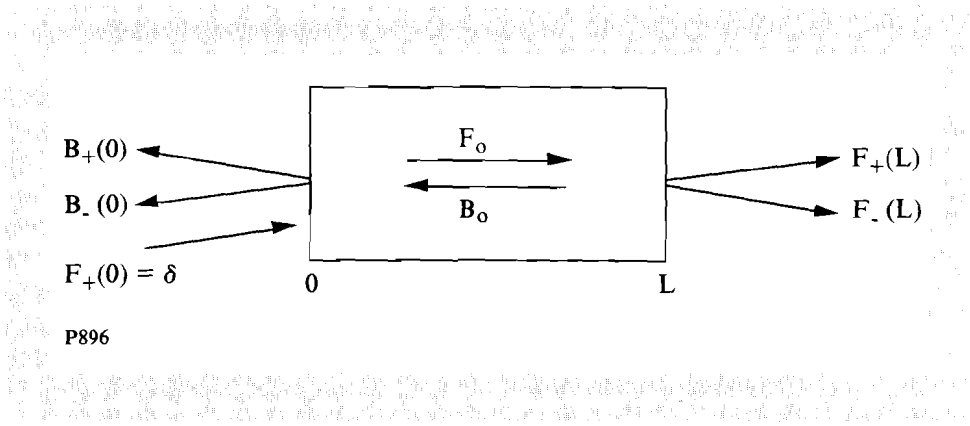

Fig. 46.5
A probe sideband seeds the convective gain and scatters into four sidebands.

In Fig. 46.6(a), the $F_+(L)$ sideband is shown. The surface plot illustrates the gain of the F_+ sideband after one pass through the plasma for a range of input angles and frequencies. Note that gain occurs for this anti-Stokes sideband at two negative values of the frequency shift. These frequencies correspond to ion-sound-wave frequencies of the gratings. The small frequency shift corresponds to scattering from the small-k grating and the larger frequency shift corresponds to scattering from the large-k grating. Their frequency shifts are given by the linear dispersion relation $\omega^2 = c_s^2 k^2$, of the ion-acoustic waves that form the gratings. At the large upshifted frequency, energy is extracted from the F_+ sideband. This is due to the resonantly enhanced interaction of the F_+ sideband with the B_+ sideband through Bragg reflection.

In Fig. 46.6(b) the spectral gain of the B_+ sideband is shown. The shallow periodic structure is due to nonresonant Bragg reflection. Again, the splitting in frequency that occurs for small frequency-shifted gain is due to the

resonant grating at $(\omega, \pm\boldsymbol{k}_\perp)$. The other two structures are present because of the grating at $(\omega, 2\boldsymbol{k}_0 \pm \boldsymbol{k}_\perp)$. The frequency-upshifted gain is caused by resonantly enhanced Bragg reflection. The large frequency-downshifted gain is due to Brillouin-like backward four-wave mixing.

The spectral gain of the Stokes-shifted F_- sideband is shown in Fig. 46.6(c). The gain in this figure represents resonantly enhanced forward four-wave mixing. The small periodic ripples, independent of ω, correspond to the nonresonant forward four-wave-mixing interaction.

Finally, the gain of the B_- sideband forming the phase-conjugate interaction with the F_+ probe is shown in Fig. 46.6(d). It is important to note that the major contribution of the back-scattered light for these parameters comes from this backward four-wave-mixing interaction. This sideband is dominated by light that scatters off-axis and is shifted by the larger ion-acoustic frequency.

This convective gain analysis reveals the complexity of the four-sideband interaction. Only in certain special limits can the four-sideband interaction be simplified to a two-sideband interaction. These limits make sense only in experiments, such as those dealing with phase conjugation, where there is some external control over which modes are seeded and which gratings are driven. In most laser-plasma interaction experiments no such control is possible.

Absolute-Instability Thresholds

As the intensities of the counterpropagating pump waves are increased, the four-sideband interaction becomes absolutely unstable. Absolute instabilities arise when nontrivial solutions of the linear four-sideband equations occur even in the absence of the seed sideband $F_+(0)$. On the top graph of Figs. 46.7(a) and 46.7(b), the thresholds for the absolute instabilities measured in units of convective gain lengths and plotted as a function of the transverse perturbation wave number are shown. For a plasma typical of that produced in the experiments by Young *et al.*,[23] a convective gain length $\gamma_0 L/v = 1$ corresponds to a pump intensity $I_0 \cong 10^{14}$ W/cm^{-2}. The four-sideband system is unstable in the shaded areas.

On the lower graph of Figs. 46.7(a) and 46.7(b), the real part of the perturbation frequency at threshold is plotted. Both figures are calculated for the case of symmetric pumps and show the data for the nonresonant threshold as a solid black line. In a nonresonant medium, a band of wave numbers centered about $k_\perp^2 L/2k_0 = 3.1$ has the lowest absolute-instability threshold. At threshold these modes are not frequency shifted with respect to the pumps. The peak of this band of wave numbers varies with the wavelength of the pump and the scale length of the medium and results from the synchronous coupling of all four sidebands. This is the four-sideband transverse modulational instability. It can be viewed as self-induced diffraction and can lead to filamentation. At large $k_\perp$ this threshold scales as $\pi|F_0|/4|B_0|$, the absolute-instability threshold for phase conjugation. In this large-$k_\perp$ region

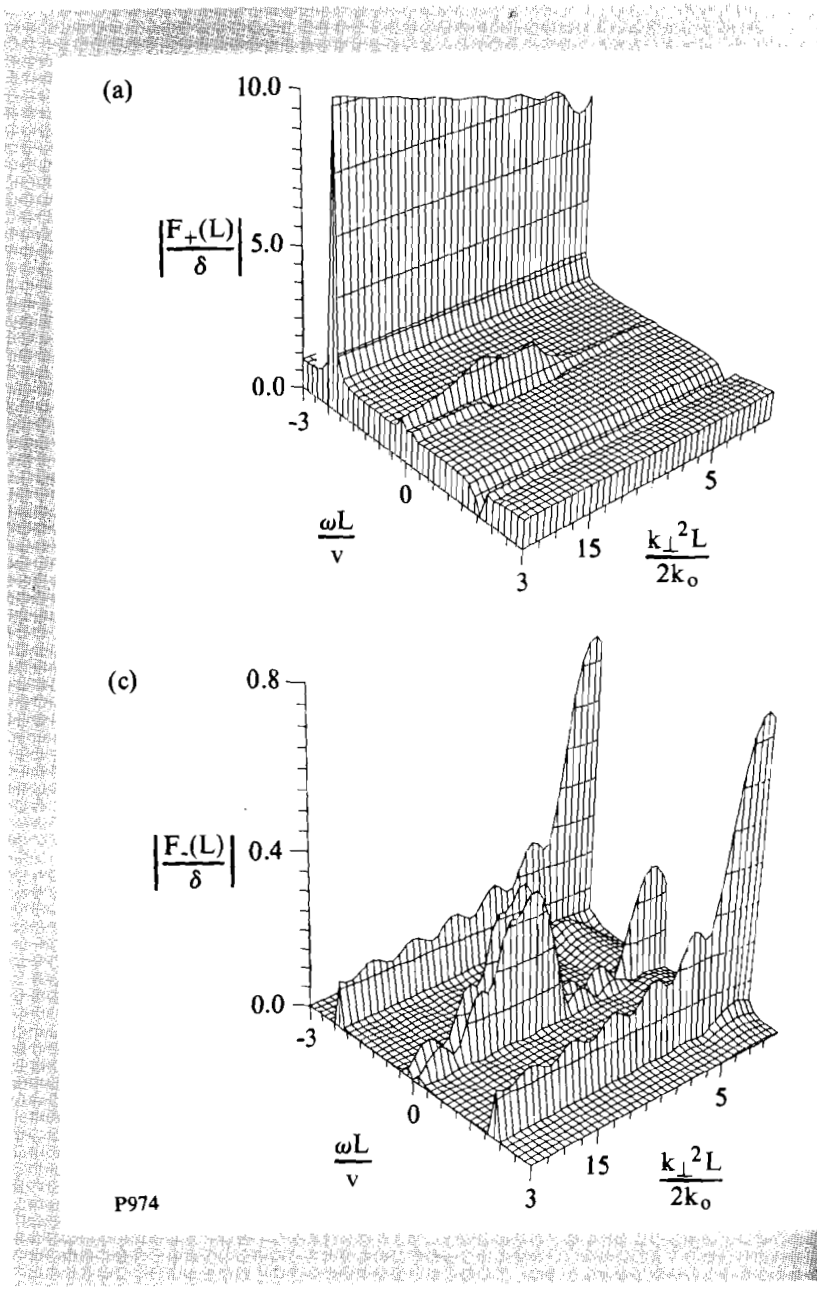

Fig. 46.6
The gain spectrum for the four sideband interaction at $\gamma_o L/v = w_e^2|F_0|^2 L/8\omega_0 v = 0.22$ is seeded by $F_+(0) = 0.001$; $|F_0| = |B_0|$, and $\gamma = 0.05$; (a) F_+, (b) B_+, (c) F^*_-, (d) B^*_-.

the oscillation frequency of the instability at the threshold for absolute instability is proportional to the difference between the pump intensities.

The dashed lines in Figs. 46.7(a) and 46.7(b) are the thresholds for the resonant absolute instabilities. In Fig. 46.7(a) the damping of the ion waves is large enough so that the nonresonant modes still dominate. In Fig. 46.7(b) the ion-acoustic wave damping has been decreased. As a result, the resonant absolute-instability branch has the lowest threshold. In both cases, the resonantly unstable modes have finite frequency shifts at threshold. In Fig. 46.7(a) this frequency shift is precisely the shift associated with the acoustic-wave frequency of the $(\omega, 2\boldsymbol{k}_o \pm \boldsymbol{k}_\perp)$ grating. In Fig. 46.7(b) a splitting about

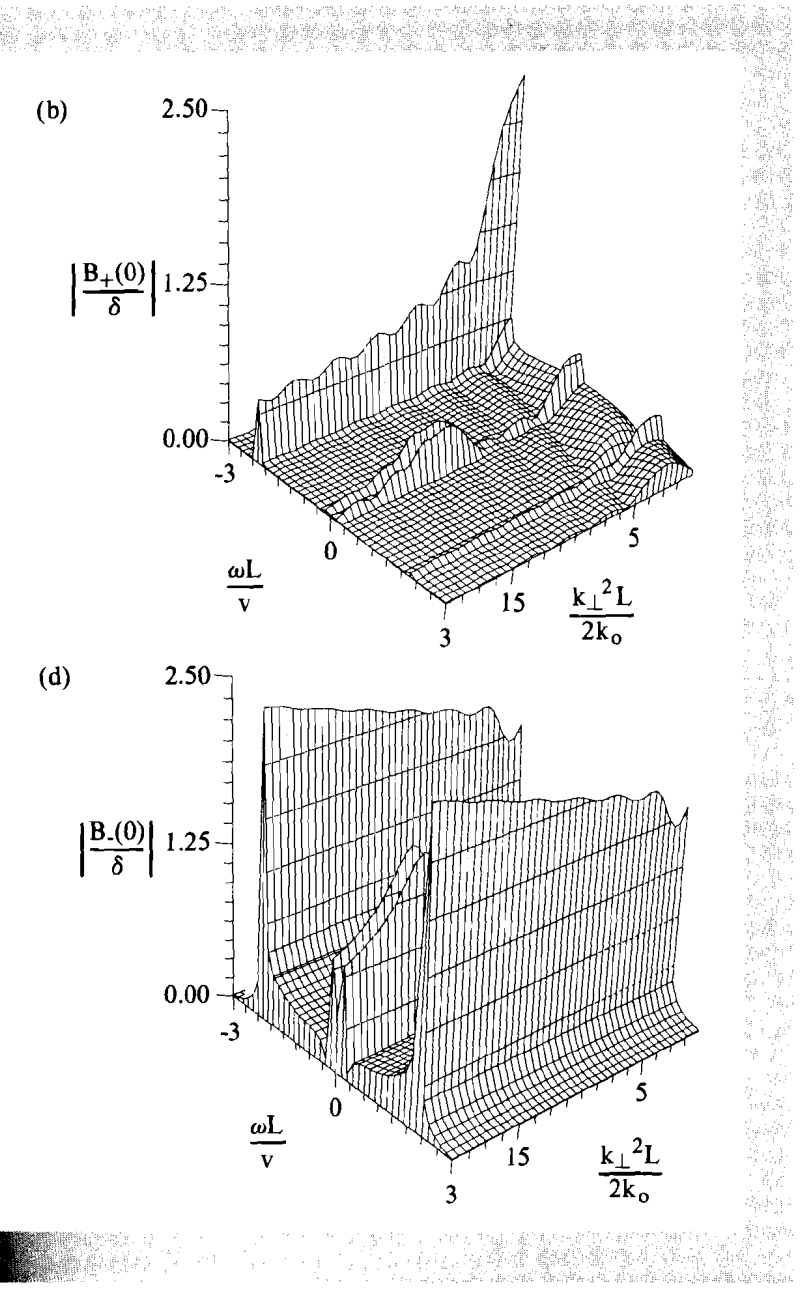

the acoustic-wave frequency can be resolved. Each value of the frequency corresponds to one of the two resonant-threshold curves. Note that neither sign of the acoustic frequency shift is favored in either figure. This occurs because the system is invariant to rotations about the pump axis and both Stokes and anti-Stokes sidebands are retained in the analysis. This symmetry is a fundamental property of the system allowing the sidebands to couple simultaneously through a shared set of gratings. The resonant absolute-instability thresholds approach the phase-conjugate threshold at large $k_\perp$. Goldman and Williams have studied the resonant absolute instability for phase conjugation in inhomogeneous plasmas with asymmetric pumping.[21] Near $k_\perp = 0$, the resonant threshold takes on a hybrid character; a result of a

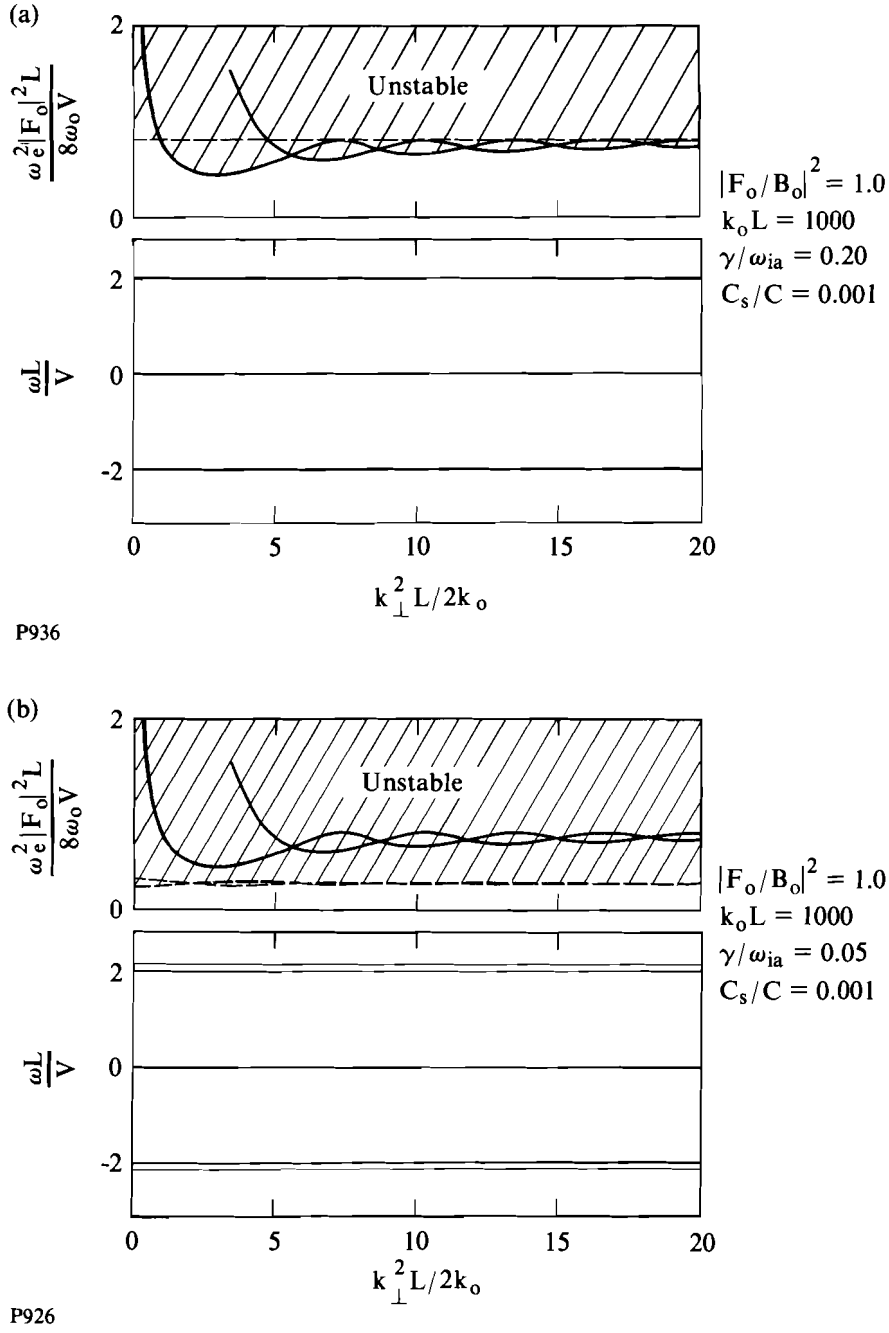

Fig. 46.7
The four-sideband interaction is absolutely unstable in the shaded regions in the top graph, and the frequency of the absolutely unstable sidebands at threshold is shown in the lower graph for each figure. In (a) $\gamma = 0.20$, and in (b) $\gamma = 0.05$. The dashed lines correspond to resonant absolute-instability modes at threshold and the solid lines correspond to nonresonant absolutely unstable modes at threshold.

combination of two-sideband interactions. In fact it is this on-axis resonance at which Fig. 46.7(b) shows the lowest absolute instability threshold.

Since the counterpropagating pump field is only a fraction of the incident pump field in inertial confinement applications, it is of particular interest to know what effect the imbalance of the pump-wave intensities has on these absolute thresholds. In Fig. 46.8 the minimal value of the absolute-instability threshold is plotted as a function of $|B_o/F_o|^2$ for two values of the ion-acoustic wave damping. For the nonresonant threshold, the small-$k_\perp$ threshold is the global minimum until very small values of $|B_o/F_o|^2$ are reached. At these values the large-$k_\perp$ phase-conjugate threshold is the minimum absolute-instability threshold. For $\gamma = 0.2$ the minimal threshold corresponds to the nonresonant curve except at very small values of $|B_o/F_o|^2$. This $\gamma = 0.2$ curve corresponds to $k_\perp = 0$. When $\gamma = 0.05$, the minimal threshold is a result of the resonant threshold and takes on a global minimum at $k_\perp = 0$. The second curve for this value of the ion-acoustic wave damping corresponds to the second threshold at $k_\perp = 0$. In general, the absolute-instability threshold is relatively insensitive to $|B_o/F_o|^2$ until it approaches zero. At $|B_o/F_o|^2 = 0$ the two pumps de-couple and no absolute instabilities can arise. From this figure it is clear that only a fraction of the incident light needs to be back-scattered before the four-sideband instabilities become important.

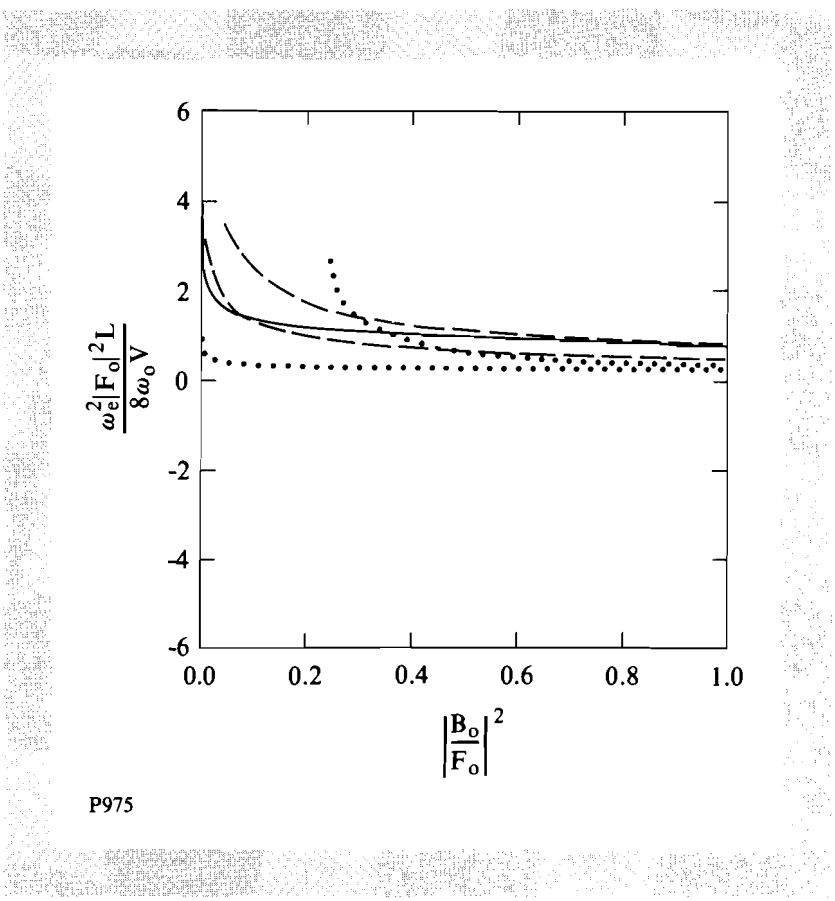

Fig. 46.8
The variation of the minimum absolute-instability threshold with the ratio of backward to forward pump intensity $|B_o/F_o|^2$ is shown. The dashed curves correspond to nonresonant absolute-instability thresholds. The lower dashed curve corresponds to the minimal threshold near $k_\perp^2 L/2k_o = 3.1$, while the higher dashed curve corresponds to $k_\perp^2 L/2k_o = 60.0$. The dotted curves correspond to resonant absolute-instability thresholds at $\gamma = 0.05$ and $k_\perp^2 L/2k_o = 0$. The solid curve corresponds to the resonant absolute-instability threshold at $\gamma = 0.20$ and $k_\perp^2 L/2k_o = 0$.

Discussion

Above the absolute threshold, when the gratings are heavily damped, the four-sideband transverse modulational instability results in conical emission since the instability grows from noise-level seed sidebands that have no preferred orientation. Several recent experiments have been done using nonresonant media exhibiting the characteristics of the four-sideband instability.[24] It is likely that the resonant instabilities will also be identified since they are so closely related to well-known instabilities. For plasma conditions typical of laser-plasma interaction experiments, this simple model predicts threshold intensities of the same magnitude as the intensities typically realized. In fact, these thresholds are much lower than those estimated for the convective-filamentation instability.

The primary near-forward and near-backward scattering instabilities that occur during the interaction of two intense counterpropagating light waves result from the planar four-sideband interactions composed of several distinct one- and two-sideband interactions. A true four-sideband instability occurs when the four sidebands and two pumps are simultaneously phase matched. The four-sideband transverse modulational instability dominates the interaction in nonresonant media. In a plasma the four-sideband resonance is still present, but both the resonantly enhanced phase-conjugate interaction and an on-axis hybrid instability resulting from the simultaneous resonantly enhanced interaction of the two types of forward four-wave mixing are also important. This latter hybrid instability has the lowest absolute-instability threshold for small values of the ion-acoustic wave damping. The instabilities arising as a result of the coupling between counterpropagating waves dominate the single-wave instabilities and require only a fraction of the incident laser to be back-scattered. Thus, the second pump wave increases the number of channels by which the laser energy is converted into unstable modes, increasing the gain of unstable sideband modes.

In laser-produced plasmas of interest for inertial confinement fusion, inhomogeneity, ion inertia, thermal effects, the time dependance of the laser pulse, and velocity gradients of the plasma will all have fundamentally important effects on the four-sideband interaction. As a result, more detailed studies must be carried out before a clear understanding of the role of four-sideband instabilities in ICF emerges.

ACKNOWLEDGMENT

This work was supported by the National Science Foundation under contract No. 9507093, by the U.S. Department of Energy Division of Inertial Fusion under agreement No. DE-FC03-85DP40200 and by the Laser Fusion Feasibility Project at the Laboratory for Laser Energetics, which has the following sponsors: Empire State Electric Energy Research Corporation, New York State Energy Research and Development Authority, Ontario Hydro, and the University of Rochester.

REFERENCES

1. C. E. Max, *Physics of Laser Fusion Volume I:* "Theory of the Coronal Plasma in Laser Fusion Targets," UCRL-53107 (1982).

2. R. L. McCrory and J. M. Soures, *Laser-Induced Plasmas and Applications*, edited by L. J. Radziemski and D. A. Cremers (Dekker, New York, 1989), Chap. 5.

3. J. F. Drake *et al.*, *Phys. Fluids* **17**, 778 (1974).

4. B. I. Cohen and C. E. Max, *Phys. Fluids* **22**, 1115 (1979).

5. W. L. Kruer, *The Physics of Laser Plasma Interactions* (Addison-Wesley, New York, 1988), Chap. 13.7, pp. 168–177.

6. H. A. Rose, D. F. DuBois, and B. Bezzerides, *Phys. Rev. Lett.* **58**, 2547 (1987).

7. D. M. Villeneuve, H. A. Baldis, and J. E. Bernard, *Phys. Rev. Lett.* **59**, 1585 (1987).

8. H. A. Baldis *et al.*, *Phys. Rev. Lett.* **62**, 2829 (1989).

9. I. M. Begg and R. A Cairns, *J. Phys. D: Appl. Phys.* **9**, 2341 (1976).

10. C. J. Randall, J. J. Thomson, and K. G. Estabrook, *Phys. Rev. Lett.* **43**, 924 (1979).

11. C. J. Randall and J. R. Albritton, *Phys. Fluids* **24**, 1474 (1981).

12. P. Narum, A. L. Gaeta, M. D. Skeldon, and R. W. Boyd, *J. Opt. Soc. Am. B* **5**, 623 (1988), and references therein.

13. A. L. Gaeta, M. D. Skeldon, R. W. Boyd, and P. Narum, *J. Opt. Soc. Am. B* **6**, 1709 (1989).

14. F. W. Perkins and E. J. Valeo, *Phys. Rev. Lett.* **32**, 1234 (1974).

15. S. N. Vlasov and E. V. Sheinina, *Izv. Vyssh. Uchebn. Zaved. Radiofiz.* **26**, 20 (1983); *Radiophys. Quantum Electron.* **26**, 15 (1983).

16. W. J. Firth and C. Paré, *Opt. Lett.* **13**, 1096 (1988).

17. G. Grynberg and J. Paye, *Europhys. Lett.* **8**, 29 (1989).

18. W. J. Firth, A. Fitzgerald, and C. Paré, *J. Opt. Soc. Am. B* **7**, 1087 (1990).

19. C. J. McKinstrie and G. G. Luther, *Phys. Scr.* **T-30**, 31 (1990).

20. G. G. Luther and C. J. McKinstrie, *J. Opt. Soc. Am.* B **7**, 1125 (1990).

21. M. V. Goldman and E. A. Williams, "Time-Dependent Phase Conjugation and Four-Wave Mixing in Plasmas," submitted to *Phys. Fluids*, and references therein.

22. H. A. Rose, D. F. DuBois, and D. Russell, *Fiz. Plazmy* **16**, 926 (1990). English language version available as Los Alamos report LA-UR-89-3349.

23. P. E. Young *et al.*, *Phys. Rev. Lett.* **61**, 2336 (1988).

24. A bibliography of related experimental papers is given in Ref. 20.